Confined growth of silver-copper Janus nanostructures with {100} facets for highly selective tandem electrocatalytic carbon dioxide reduction

Yangbo Ma,[1,†] Jinli Yu,[1,†] Mingzi Sun,[3,†] Bo Chen,[1,†] Xichen Zhou,[1] Chenliang Ye,[4] Zhiqiang Guan,[1,9] Weihua Guo,[1] Gang Wang,[5] Shiyao Lu,[1] Dongsheng Xia,[6] Yunhao Wang,[1] Zhen He,[1,2] Long Zheng,[5] Qinbai Yun,[1] Jingwen Zhou,[1,2] Pengyi Lu,[1,2] Jinwen Yin,[1] Yifei Zhao,[1,2] Zhongbin Luo,[1] Li Zhai,[1,2] Lingwen Liao,[1,8] Ruquan Ye,[1] Ye Chen,[5] Shibo Xi,[7,*] Bolong Huang,[3,*] Chun-Sing Lee,[1,9] and Zhanxi Fan[1,2,10,*]

[1]Department of Chemistry, City University of Hong Kong, Hong Kong, China.

[2]Hong Kong Branch of National Precious Metals Material Engineering Research Center (NPMM), City University of Hong Kong, Hong Kong, China.

[3]Department of Applied Biology and Chemical Technology, The Hong Kong Polytechnic University, Hong Kong, China.

[4]Department of Chemistry, Tsinghua University, Beijing 100084, China.

[5]Department of Chemistry, The Chinese University of Hong Kong, Hong Kong, China.

[6]Institute of Materials Research and Shenzhen Geim Graphene Research Centre, Tsinghua Shenzhen International Graduate School, Tsinghua University, Shenzhen 518055, China.

[7]Institute of Chemical and Engineering Sciences, A*STAR, Singapore 627833, Singapore.

[8]Key Laboratory of Materials Physics, Anhui Key Laboratory of Nanomaterials and Nanotechnology, Institute of Solid State Physics, Chinese Academy of Sciences, Hefei, 230031, China.

[9]Center of Super-Diamond and Advanced Films (COSDAF), City University of Hong Kong, Hong Kong, China.

[10]Shenzhen Research Institute, City University of Hong Kong, Shenzhen, 518057, China.

[†]These authors contributed equally to this work.

*Corresponding authors.

E-mail: zhanxi.fan@cityu.edu.hk; hua.zhang@cityu.edu.hk; bhuang@polyu.edu.hk; xi_shibo@nus.edu.sg

ABSTRACT

Electrochemical carbon dioxide reduction reaction (CO_2RR) holds significant potential to promote carbon neutrality as it can convert CO_2 to value-added chemicals/fuels with intermittent renewable electricity. However, the Faradaic efficiency of multi-carbon products in CO_2RR is still too low to meet practical applications. Here we first report the synthesis of three kinds of Ag-Cu Janus nanostructures with {100} facets (JNS-100) for highly selective tandem electrocatalytic reduction of CO_2 to multi-carbon products. By controlling the surfactant and reduction kinetics of Cu precursor, we realize the confined growth of Cu with {100} facets on only one of the six equal faces of Ag nanocubes. Compared with Cu nanocubes, Ag_{65}-Cu_{35} JNS-100 demonstrates much superior selectivity toward both ethylene and multi-carbon products in CO_2RR at less negative potentials. Density functional theory calculations reveal that the compensating electronic structure and carbon monoxide spillover in Ag_{65}-Cu_{35} JNS-100 contributes to the enhanced CO_2RR performance. This study provides an effective strategy to design advanced tandem catalysts toward the real application of CO_2RR.

INTRODUCTION

Owing to its excellent compatibility with the intermittent renewable electricity, electrochemical carbon dioxide reduction reaction (CO_2RR) is considered as a promising strategy to reduce the excessively accumulated CO_2 in earth atmosphere and promote carbon neutral.[1-5] In CO_2RR, CO_2 can be converted to a series of value-added chemicals and fuels, including single-carbon (C_1) products (e.g., carbon monoxide (CO), formate ($HCOO^-$), methane (CH_4) and methanol (CH_3OH)) and multi-carbon (C_{2+}) products (e.g., ethylene (C_2H_4), ethanol (C_2H_5OH), ethane (C_2H_6) and n-propanol (n-C_3H_7OH)).[6-12] Among these products, C_{2+} products like C_2H_5OH and C_2H_4 have attracted extraordinary interest since they are either essential fuels with high energy density or core chemical feedstocks with large economic value. To date, copper (Cu) is the most distinctive catalyst that can facilitate the reduction of CO_2 to various C_{2+} products with a promising Faradaic efficiency (FE).[13-17] However, the FE of C_{2+} products on current Cu-based catalysts remains too low to meet the practical applications.[4,15]

Very recently, increasing efforts have been made to prepare novel Cu-based CO_2RR catalysts for C_{2+} products.[18-23] Among various strategies, constructing tandem catalysts is emerging as a feasible approach to further improve the FE of C_{2+} products.[24-33] In the tandem catalytic system, the first kind of metal (e.g., silver (Ag),[24,26,30,34] gold (Au),[29,31] and palladium (Pd)[25,35]) is able to convert CO_2 to CO at lower overpotentials compared to that on Cu. Then the obtained CO spills over to the nearby Cu sites,[31,36] where CO will be further reduced to C_{2+} products via the carbon-carbon (C-C) coupling process.[24,26,32] In addition, the facet of the nanoparticle, which can significantly affect the final products of CO_2RR,[37-40] should also be considered in the design of advanced

tandem catalysts. Experimental and theoretical studies suggested that Cu (100) plane favors the generation of C_2H_4 over the Cu (111) plane because Cu (100) plane possesses a lower energy barrier for C-C coupling.[40-45] However, although a range of Cu-based tandem catalysts has been prepared for CO_2RR, the Cu domains in those previously reported heteronanostructure ones usually do not have specific exposed facets especially {100} facets,[25,26,29,46] resulting in a limited C_{2+} selectivity.

In this work, for the first time, via the rational control of surfactant and reduction kinetics of Cu precursor, we synthesize three kinds of Ag-Cu Janus nanostructures with {100} facets (JNS-100). These Ag-Cu JNS-100 are all highly active tandem catalysts toward the electrochemical reduction of CO_2 to C_{2+} products. In particular, Ag_{65}-Cu_{35} JNS-100 can effectively convert CO_2 to C_2H_4 and C_{2+} products with excellent FE of 54% and 72%, respectively. Density functional theory (DFT) calculations have unraveled the electronic structure evolution induced by the different Ag/Cu ratios in the Ag-Cu tandem catalysts. Ag_{65}-Cu_{35} JNS-100 demonstrates the highest selectivity toward C_{2+} products due to the suitable electronic structure and the tandem effect induced by CO spillover.

RESULTS AND DISCUSSION

As shown in Figure 1a, Ag-Cu Janus nanostructures with {100} facets (JNS-100) were synthesized through the confined growth of Cu on Ag nanocubes (NCs, with a size of 41.8 ± 4.7 nm, Figure S1) by controlling the surfactant and the adding speed of $CuCl_2{\cdot}2H_2O$ and L-ascorbic acid (see "Supporting Information" for details). By systematically adjusting the amount and adding speed of Cu precursors, three kinds of Ag-Cu JNS-100 with different Ag/Cu atomic ratios, including Ag_{65}-Cu_{35}, Ag_{50}-Cu_{50} and Ag_{75}-Cu_{25}, were obtained (Figure S2). As a control sample for the catalytic

performance measurement, pure Cu NCs with an edge length of 42.5 ± 5.7 nm were also synthesized (Figure S3).

Transmission electron microscopy (TEM) images of Ag_{65}-Cu_{35} JNS-100 reveal that the Cu domains grow on only one of the six equal faces of Ag NCs (Figure 1b,c and Figure S4a,b). Figure 1d shows a representative spherical aberration-corrected high-resolution high-angle annular dark-field scanning TEM (HAADF-STEM) image of the Ag/Cu interface in Ag_{65}-Cu_{35} JNS-100, indicating the epitaxial growth of the Cu domains on Ag NCs. Selected-area fast Fourier transform (FFT) patterns of the Ag domain, Cu domain and Ag/Cu interface in Figure 1d all match well with the typical electron diffraction patterns of face-centered cubic (fcc) phase along the $[001]_f$ zone axis (Figure 1e-g). This also suggests that the six faces of Ag_{65}-Cu_{35} JNS-100 are enclosed by fcc {100} facets. Figure 1h demonstrates the integrated pixel intensities of the marked Ag and Cu domains along the directions denoted in Figure 1d. The average interplanar spacings of Ag and Cu domains were calculated to be 1.96 Å and 1.78 Å, which are assigned to the fcc Ag ($\bar{2}00$) and fcc Cu ($\bar{2}00$) planes, respectively.

The HAADF-STEM image and corresponding energy-dispersive X-ray spectroscopy (EDS) elemental mapping of Ag_{65}-Cu_{35} JNS-100 further prove that Cu selectively grows on only one face of Ag NCs, leading to the formation of well-defined Ag-Cu Janus nanostructures (Figure 1i,j). Moreover, the obtained Ag_{50}-Cu_{50} JNS-100 and Ag_{25}-Cu_{75} JNS-100 also exhibit well-defined Janus nanostructures, as determined by the TEM, HAADF-STEM and EDS mapping (Figure S4c,d, Figure S5a,b, Figure S6a,b and Figure 1k-n). Spherical aberration-corrected high-resolution STEM images and corresponding selected-area FFT patterns (Figure S5c-e and Figure S6c-e) identify the

epitaxial growth of Cu on Ag NCs, as well as the exposure of fcc {100} facets for both Ag_{50}-Cu_{50} JNS-100 and Ag_{25}-Cu_{75} JNS-100.

X-ray diffraction (XRD) was also used to characterize the structure of as-synthesized Ag-Cu JNS-100. As shown in Figure 2a, the peak positions of Ag and Cu in the XRD patterns of three kinds of Ag-Cu JNS-100 are all well consistent with those of pure Ag NCs and pure Cu NCs, respectively, which further confirms the successful formation of Ag-Cu Janus nanostructures. Figure S7 shows that both Ag domains and Cu domains in the obtained Ag-Cu JNS-100 adopt the standard fcc phase, matching well with the spherical aberration-corrected high-resolution STEM results (Figure 1d-g, Figure S5c-e and Figure S6c-e).

The surface status of as-synthesized Ag-Cu JNS-100 was analyzed by X-ray photoelectron spectroscopy (XPS). As shown in Figure 2b, the Ag 3d peaks of Ag domains shift to higher binding energy after forming the Ag-Cu Janus nanostructures, suggesting the existence of electron transfer from the Ag domains to the Cu domains via the Ag/Cu interface.[28,47,48] For the lower Cu content results in the larger binding energy shift, it might be related to the relative ratio of the Ag/Cu interface to the Cu content in Ag-Cu JNS-100. For the corresponding XPS spectra of Cu 2p (Figure 2c), they demonstrate a consistent peak shift with the electron transfer between the Ag domains and Cu domains. Besides, the appearance of weak satellite peaks in Cu 2p XPS spectra indicates the slight oxidation of Cu in air.

X-ray absorption spectroscopy (XAS) was further utilized to probe into the electronic and geometric structures of Ag-Cu JNS-100. In the Cu K edge X-ray absorption near-edge structure (XANES) (Figure 2d), the white line intensity of Cu NCs, Ag_{65}-Cu_{35} JNS-100 and Ag_{25}-Cu_{75} JNS-100 is a slightly higher than that of Cu foil, suggesting the

slight oxidation of surface Cu atoms in Cu NCs and Ag-Cu JNS-100. k^2-weighted R-space extended X-ray absorption fine structure (EXAFS) was employed to investigate the local structure of Cu. As shown in Figure 2e, the Cu foil shows a main peak at R of ~ 2.20 Å, which is attributed to Cu-Cu scatterings of the first shell. The Cu-Cu scattering peaks were also observed in the Cu NCs, Ag_{65}-Cu_{35} JNS-100 and Ag_{25}-Cu_{75} JNS-100, indicating the formation of Cu-Cu bonds in these samples. As listed in Table S1, the Cu-Cu coordination numbers of Cu NCs, Ag_{65}-Cu_{35} JNS-100 and Ag_{25}-Cu_{75} JNS-100 are 9.2, 8.5 and 7.4, respectively, which are lower than that of Cu foil. This might result from the size effect and the oxidized surface Cu atoms that reduce the average Cu-Cu coordination numbers.[49,50] Importantly, the Cu-Cu coordination numbers in Cu NCs, Ag_{65}-Cu_{35} JNS-100 and Ag_{25}-Cu_{75} JNS-100 are all significantly larger than those of Cu-O coordination numbers, revealing that the metallic Cu is the dominant component. In the Ag L_3 edge XANES (Figure 2f), the white line intensity of both Ag_{65}-Cu_{35} JNS-100 and Ag_{25}-Cu_{75} JNS-100 are higher than that of Ag NCs, suggesting a higher chemical state of Ag in Ag-Cu JNS-100 samples. This could be caused by the electron transfer from the Ag domain to the Cu domain within Ag-Cu JNS-100, which is consistent with the XPS results (Figure 2b). Wavelet transform was applied to investigate the coordination environment of the Cu species in samples. As shown in Figure 2g-i, the intensity maxima of Cu NCs, Ag_{65}-Cu_{35} JNS-100 and Ag_{25}-Cu_{75} JNS-100 are very close, confirming that the Cu-Cu bonds are dominant in all these samples, matching well with the R-space EXAFS fitting results (Figure S8).

The CO_2RR performance of as-prepared three kinds of Ag-Cu JNS-100 was investigated in a gas-tight H-type cell under ambient conditions. The CO_2-saturated 0.1 M $KHCO_3$ and glass carbon electrode were used as electrolyte and working electrode support, respectively. All the applied potentials in this work were recorded without

solution resistance correction (see "Supporting Information" for details). For comparison, the CO_2RR performance of Ag NCs, Cu NCs and the physical mixture of Ag NCs and Cu NCs (denoted as "Ag+Cu mixture", Figure S9) was also tested under the same conditions. As shown in Figure 3a-c, Ag_{65}-Cu_{35}, Ag_{50}-Cu_{50} and Ag_{25}-Cu_{75} JNS-100 all exhibited C_2H_4 FE over 50% at their optimal potentials, indicating their excellent catalytic selectivity toward C_{2+} products in CO_2RR. Note that the three Ag-Cu Janus nanostructures exhibited similar partial current densities toward the production of C_2H_4, as shown in Figure S10. In particular, Ag_{65}-Cu_{35} JNS-100 exhibited over 50% FE of C_2H_4 in a wide potential window from -1.0 V to -1.4 V (vs reversible hydrogen electrode (RHE)). At -1.2 V (vs RHE), Ag_{65}-Cu_{35} JNS-100 demonstrated the highest FE of 54% for C_2H_4. In contrast, at -1.2 V (vs RHE), Cu NCs showed FE of only 45% for C_2H_4 (Figure S11a). The main product for Ag NCs and Ag+Cu mixture was CO at the potentials from -0.8 V to -1.4 V (vs RHE) (Figure S11b,c). Besides C_2H_4, other C_{2+} products including C_2H_5OH, acetate, n-C_3H_7OH, acetaldehyde and acetone were also observed on the Ag-Cu JNS-100 (Table S2-4). Remarkably, Ag_{65}-Cu_{35} JNS-100 displayed a FE of 67% for C_{2+} products at -1.2 V (vs RHE), which is much higher than those of Cu NCs (52%) and Ag+Cu mixture (22%) (Figure 3d). At -1.4 V (vs RHE), Ag_{65}-Cu_{35} JNS-100 achieved the highest FE of 72% for C_{2+} products (Table S2). Therefore, in comparison with the previously reported Cu-based catalysts for CO_2RR, the FE of Ag_{65}-Cu_{35} JNS-100 is among the best toward ethylene and C_{2+} products (Table S5).

To understand the superior CO_2RR performance of Ag_{65}-Cu_{35} JNS-100, we compared the applied potentials for producing C_2H_4 with considerable FE, which is closely related to the cathode energy efficiency of catalysts,[51,52] between Ag_{65}-Cu_{35} JNS-100 and Cu NCs (Figure 3e). In the less negative potential range of -0.8 V to -1.4 V (vs RHE), Ag_{65}-

Cu_{35} JNS-100 showed much higher C_2H_4 FE than Cu NCs. Significantly, the potential to reach over 50% FE for C_2H_4 on Ag_{65}-Cu_{35} JNS-100 was reduced about 400 mV when compared with pure Cu NCs, resulting in the much higher cathode energy efficiency on Ag_{65}-Cu_{35} JNS-100 than that on Cu NCs toward C_2H_4 production (Figure S12). Furthermore, the C_{2+}/C_1 product ratio among Ag_{65}-Cu_{35} JNS-100, Cu NCs and Ag+Cu mixture was also compared, which is closely related to the C-C coupling process[53-55] (Figure 3f). Ag_{65}-Cu_{35} JNS-100 exhibited the highest C_{2+}/C_1 product ratios from -1.0 V to -1.6 V (vs RHE). Impressively, the highest C_{2+}/C_1 product ratio of 4.8 was achieved on Ag_{65}-Cu_{35} JNS-100 at -1.4 V (vs RHE), which is 1.5 and 4.8 times of Cu NCs (3.3) and Ag+Cu mixture (1.0), respectively. These results reveal that Ag_{65}-Cu_{35} JNS-100 possesses excellent catalytic selectivity toward C_{2+} products in CO_2RR.

The improved CO_2RR performance of Ag-Cu JNS-100 is largely attributed to the exposed Cu {100} facets, the Janus nanostructure-induced tandem catalysis, and the electron transfer between Ag and Cu domains. For the Cu {100} facets (Figure 1d-h), theoretical and experimental works have verified that they can reduce the energy barrier for the C-C coupling and improve the selectivity toward C_2H_4.[40-44] As for the Janus nanostructures of Ag-Cu JNS-100, the Ag domain is able to reduce CO_2 to CO with much higher FE than Cu at low potentials, which has been confirmed by comparing the CO_2RR performance of pure Cu NCs and pure Ag NCs (Figure S11a,b). The obtained CO could spill over from Ag domain to the adjacent Cu domain (will be discussed in detail later) and be further reduced to C_{2+} products, which would account for the reduced potential of producing considerable C_2H_4 on Ag-Cu JNS-100 (Figure 3e). Simultaneously, the spillovered CO can change the CO coverage on Cu surface, which could reduce the energy needed for C-C coupling on Cu (100) plane[36,38,56] and thus contribute to the improved C_2H_4 FE and C_{2+}/C_1 product ratio. As for the electron

transfer between Ag and Cu in Ag-Cu JNS-100 (Figure 2b,c), its effect on CO_2RR performance will be further discussed later. Taken together, a plausible CO_2RR mechanism on Ag-Cu JNS-100 is schematically illustrated in Figure 3g.

The catalytic stability of Ag_{65}-Cu_{35} JNS-100 was also evaluated by the long-term CO_2 electrolysis at the constant potential. As shown in Figure S13, after electrolysis at -1.2 V (vs RHE) for almost 10 h, the FE of C_2H_4 on Ag_{65}-Cu_{35} JNS-100 only demonstrated a slight decrease. Meanwhile, no obvious change in the current density was observed. TEM image of Ag_{65}-Cu_{35} JNS-100 after the stability test shows that although some Cu domains have been partially etched, most of the Ag_{65}-Cu_{35} JNS-100 still well maintain their morphology and Janus nanostructures (Figure S14), suggesting the good catalytic durability of Ag_{65}-Cu_{35} JNS-100 toward electrocatalytic CO_2RR.

To better understand the CO_2RR performance of Ag-Cu JNS-100, we have applied the DFT calculations to investigate the electronic structures and reaction trends. Notably, the different concentrations of Ag and Cu have significantly modulated the surface electronic distributions (Figure S15). For the Ag_{65}-Cu_{35} JNS-100, we notice that both Ag and Cu contribute to the bonding orbitals, especially the interface regions have also been activated (Figure S15a). Similar electronic distributions are also noted in the Ag_{50}-Cu_{50} JNS-100 (Figure S15b). As the content of Cu becomes higher in the Ag_{25}-Cu_{75} JNS-100, the Cu domain dominates the bonding orbitals while the Ag domain mostly shows the anti-bonding orbitals (Figure S15c). Then, we further compare the electronic structures in three Ag-Cu JNS-100 including Ag_{65}-$Cu_{35,}$ Ag_{50}-$Cu_{50,}$ and Ag_{25}-Cu_{75}. For the Cu-3d orbitals, we notice that Cu-3d orbitals display a downshifting trend with the increasing content of the Cu (Figure 4a). In particular, compared to pristine Cu, the Ag-Cu JNS-100 has shown a slightly lowered dominant peak, which supports the more

electron-rich feature in Ag-Cu JNS-100. Meanwhile, an opposite trend was found in Ag (Figure 4b). Compared to pristine Ag, all the Ag-4d orbitals in tandem catalysts demonstrate a much higher position, which indicates the higher electron valence in the structure, consistent with the XPS results (Figure 2b). Ag-4d orbitals show the overall lower position than Cu-3d orbitals, displaying as the electron reservoir during the CO_2RR.

The d-band center has been calculated for different Ag-Cu JNS-100, pristine Ag and pristine Cu (Figure 4c). Notably, pristine Ag shows a very low d-band center at E_V-5.16 eV (E_V = 0 eV), while the introduction of Cu significantly increases the d-band center. Although the higher d-band center usually leads to high electroactivity, the low selectivity toward the C_{2+} products during CO_2RR becomes another challenge. To guarantee efficient CO_2RR to generate desired C_{2+} products, an appropriate d-band center is also important. Thus the median d-band center of Ag_{65}-Cu_{35} JNS-100 displays the highest FE for C_{2+} products. Compared to the Cu (100) surface, the Cu-3d orbitals within the Ag_{65}-Cu_{35} JNS-100 display the gradual upshifting trend from the bulk at E_V-2.18 eV to the surface at E_V-1.55 eV (Figure 4d). In particular, Cu sites at the surface interface show a high electroactivity to promote the electron transfer from electron-rich Ag domains. Meanwhile, the Ag-4d orbitals also exhibit the upshifting trend from the bulk to the surface (Figure 4e). This trend facilitates the efficient electron transfer from Ag to Cu and further toward the adsorbates. For the formation of C_2H_4, the projected density of the states (PDOS) of key intermediates confirm the linear correlation of the σ orbitals in C, O species, leading to the smooth intermediate conversions (Figure 4f).

Then we further investigate the CO_2RR performance of Ag-Cu JNS-100 from the energetic perspective. From the Ag domain to the Cu domain within Ag_{65}-Cu_{35} JNS-

100, the adsorption energy of *CO gradually decreases, indicating that CO tends to spillover from the Ag surface to the Cu surface (Figure 4g). As a result, the C-C coupling processes can be promoted on the Cu domain due to CO spillover,[32,52] leading to the increased FE of C_{2+} products and C_2H_4 (Figure 3d,e). More importantly, the key adsorbate *OCCO shows the much stronger adsorptions on the Cu domain, while the high energy cost of *OCCO leads to the difficult generation of C_{2+} products on Ag surface. These results further explain the significant improvements of the C_{2+}/C_1 product ratio on Ag_{65}-Cu_{35} JNS-100 compared to pure Cu NCs (Figure 3f). Different reaction pathways have been compared on Ag_{65}-Cu_{35} JNS-100 (Figure 4h). The formation of CO from CO_2 is energetically favourable while the generation of HCOOH shows an energy barrier of 0.64 eV, explaining the low FE for HCOOH. The further hydrogenation of *CHCO to *CH_2CO shows a high energy barrier of 1.02 eV, while the conversion from *CHCO to *CHCHO shows a much lower energy barrier of 0.52 eV. The continuous uphill reaction trend from *CHCO to *CH_3COOH results in the low selectivity toward the production of acetic acid (Table S2). Meanwhile, the conversion from *CHCHO to *CH_2CH_2OH display the downhill trend, which demonstrates a high reaction trend. For the final reaction step, the formation of CH_3CH_2OH shows an energy cost of 0.52 eV while the formation of C_2H_4 is spontaneous with a total energy release of -2.52 eV. Therefore, the reaction energy of CO_2RR also reveals the high reaction preference toward specific C_{2+} products on Ag_{65}-Cu_{35} JNS-100.

CONCLUSIONS

In summary, we have successfully synthesized three kinds of Ag-Cu JNS-100 through the confined growth of Cu on only one of six equal faces of Ag NCs. The obtained Ag-

Cu JNS-100 all demonstrate excellent CO_2RR performance toward C_{2+} products. In particular, compared with Cu NCs, Ag_{65}-Cu_{35} JNS-100 not only shows superior C_2H_4 FE of 54% and C_{2+} product FE of 72 % but also exhibits significantly reduced potential for producing C_2H_4 and greatly improved C_{2+}/C_1 product ratio. DFT calculations have investigated the CO_2RR performance of Ag-Cu JNS-100 from both electronic structures and reaction energies. Ag_{65}-Cu_{35} JNS-100 has exhibited the most optimized electronic structures and promoted the CO spillover effect, which guarantees the highest selectivity and low energy barriers for the generation of C_{2+} products. It is believed that this work will not only offer new opportunities for the controlled synthesis of well-defined bimetallic Janus nanostructures but also shed light on the rational design of next-generation CO_2RR catalysts.

ACKNOWLEDGEMENTS

Y.M., J.Yu, M.S., and B.C. contributed equally to this work. This work was supported by Grants (Project No. 22005258, 22175148, and 21771156) from National Natural Science Foundation of China, the National Key R&D Program of China (2021YFA1501101), and ITC via Hong Kong Branch of National Precious Metals Material Engineering Research Center (NPMM), and Grants (Project No. 9610480, 7005512, 7005600, and 9680301) from City University of Hong Kong, and Start-Up Grant (Project No. 4930977) from The Chinese University of Hong Kong, the NSFC/RGC Joint Research Scheme (N_PolyU502/21), and the funding for Projects of Strategic Importance of The Hong Kong Polytechnic University (Project Code: 1-ZE2V). The computational work for this article was partially performed on the resources of the National Supercomputing Centre, Singapore.

CONFLICT OF INTEREST

The authors declare no competing financial interest.

REFERENCES

1. Nitopi, S.; Bertheussen, E.; Scott, S. B.; Liu, X.; Engstfeld, A. K.; Horch, S.; Seger, B.; Stephens, I. E. L.; Chan, K.; Hahn, C.; Norskov, J. K.; Jaramillo, T. F.; Chorkendorff, I. Progress and perspectives of electrochemical CO_2 reduction on copper in aqueous electrolyte. *Chem. Rev.* **2019,** *119*, 7610-7672.

2. Xie, C.; Niu, Z.; Kim, D.; Li, M.; Yang, P. Surface and interface control in nanoparticle catalysis. *Chem. Rev.* **2020,** *120*, 1184-1249.

3. Ma, Y.; Wang, J.; Yu, J.; Zhou, J.; Zhou, X.; Li, H.; He, Z.; Long, H.; Wang, Y.; Lu, P.; Yin, J.; Sun, H.; Zhang, Z.; Fan, Z. Surface modification of metal materials for high-performance electrocatalytic carbon dioxide reduction. *Matter* **2021,** *4*, 888-926.

4. Yu, J.; Wang, J.; Ma, Y.; Zhou, J.; Wang, Y.; Lu, P.; Yin, J.; Ye, R.; Zhu, Z.; Fan, Z. Recent progresses in electrochemical carbon dioxide reduction on copper-based catalysts toward multicarbon products. *Adv. Funct. Mater.* **2021,** *31*, 2102151.

5. Li, H.; Zhou, X.; Zhai, W.; Lu, S.; Liang, J.; He, Z.; Long, H.; Xiong, T.; Sun, H.; He, Q.; Fan, Z.; Zhang, H. Phase engineering of nanomaterials for clean energy and catalytic applications. *Adv. Energy Mater.* **2020,** *10*, 2002019.

6. Fan, L.; Xia, C.; Yang, F.; Wang, J.; Wang, H.; Lu, Y. Strategies in catalysts and electrolyzer design for electrochemical CO_2 reduction toward C_{2+} products. *Sci. Adv.* **2020,** *6*, eaay3111.

7. Zheng, Y.; Vasileff, A.; Zhou, X.; Jiao, Y.; Jaroniec, M.; Qiao, S. Z. Understanding the roadmap for electrochemical reduction of CO_2 to multi-carbon oxygenates and hydrocarbons on copper-based catalysts. *J. Am. Chem. Soc.* **2019,** *141*, 7646-7659.

8. Birdja, Y. Y.; Pérez-Gallent, E.; Figueiredo, M. C.; Göttle, A. J.; Calle-Vallejo, F.; Koper, M. T. M. Advances and challenges in understanding the electrocatalytic conversion of carbon dioxide to fuels. *Nat. Energy* **2019,** *4*, 732-745.

9. Lu, S.; Liang, J.; Long, H.; Li, H.; Zhou, X.; He, Z.; Chen, Y.; Sun, H.; Fan, Z.; Zhang, H. Crystal phase control of gold nanomaterials by wet-chemical synthesis. *Acc. Chem. Res.* **2020,** *53*, 2106-2118.

10. Fan, Z.; Bosman, M.; Huang, Z.; Chen, Y.; Ling, C.; Wu, L.; Akimov, Y. A.; Laskowski, R.; Chen, B.; Ercius, P.; Zhang, J.; Qi, X.; Goh, M. H.; Ge, Y.; Zhang, Z.; Niu, W.; Wang, J.; Zheng, H.; Zhang, H. Heterophase fcc-2H-fcc gold nanorods. *Nat. Commun.* **2020,** *11*, 3293.

11. Ge, Y.; Huang, Z.; Ling, C.; Chen, B.; Liu, G.; Zhou, M.; Liu, J.; Zhang, X.; Cheng, H.; Liu, G.; Du, Y.; Sun, C.-J.; Tan, C.; Huang, J.; Yin, P.; Fan, Z.; Chen, Y.; Yang, N.; Zhang, H. Phase-selective epitaxial growth of heterophase nanostructures on unconventional 2H-pd nanoparticles. *J. Am. Chem. Soc.* **2020,** *142*, 18971-18980.

12. Wang, Y.; Li, C.; Fan, Z.; Chen, Y.; Li, X.; Cao, L.; Wang, C.; Wang, L.; Su, D.; Zhang, H.; Mueller, T.; Wang, C. Undercoordinated active sites on 4H gold nanostructures for CO_2 reduction. *Nano Lett.* **2020,** *20*, 8074-8080.

13. Gawande, M. B.; Goswami, A.; Felpin, F. X.; Asefa, T.; Huang, X.; Silva, R.; Zou, X.; Zboril, R.; Varma, R. S. Cu and Cu-based nanoparticles: Synthesis and applications in catalysis. *Chem. Rev.* **2016,** *116*, 3722-3811.

14. Bagger, A.; Ju, W.; Varela, A. S.; Strasser, P.; Rossmeisl, J. Electrochemical CO_2 reduction: A classification problem. *ChemPhysChem* **2017,** *18*, 3266-3273.

15. Zhu, S.; Delmo, E. P.; Li, T.; Qin, X.; Tian, J.; Zhang, L.; Shao, M. Recent advances in catalyst structure and composition engineering strategies for regulating CO_2 electrochemical reduction. *Adv. Mater.* **2021**, DOI: 10.1002/adma.202005484.

16. Wang, Y.; Liu, J.; Zheng, G. Designing copper-based catalysts for efficient carbon dioxide electroreduction. *Adv. Mater.* **2021**, DOI: 10.1002/adma.202005798.

17. Mistry, H.; Varela, A. S.; Bonifacio, C. S.; Zegkinoglou, I.; Sinev, I.; Choi, Y.-W.; Kisslinger, K.; Stach, E. A.; Yang, J. C.; Strasser, P.; Cuenya, B. R. Highly selective plasma-activated copper catalysts for carbon dioxide reduction to ethylene. *Nat. Commun.* **2016,** *7*, 12123.

18. Chen, Y.; Fan, Z.; Wang, J.; Ling, C.; Niu, W.; Huang, Z.; Liu, G.; Chen, B.; Lai, Z.; Liu, X.; Li, B.; Zong, Y.; Gu, L.; Wang, J.; Wang, X.; Zhang, H. Ethylene selectivity in electrocatalytic CO_2 reduction on Cu nanomaterials: A crystal phase-dependent study. *J. Am. Chem. Soc.* **2020,** *142*, 12760-12766.

19. Choi, C.; Kwon, S.; Cheng, T.; Xu, M.; Tieu, P.; Lee, C.; Cai, J.; Lee, H. M.; Pan, X.; Duan, X.; Goddard, W. A.; Huang, Y. Highly active and stable stepped Cu surface for enhanced electrochemical CO_2 reduction to C_2H_4. *Nat. Catal.* **2020,** *3*, 804-812.

20. Choi, C.; Cheng, T.; Flores Espinosa, M.; Fei, H.; Duan, X.; Goddard, W. A., 3rd; Huang, Y. A highly active star decahedron Cu nanocatalyst for hydrocarbon production at low overpotentials. *Adv. Mater.* **2019,** *31*, e1805405.

21. Gu, Z.; Shen, H.; Chen, Z.; Yang, Y.; Yang, C.; Ji, Y.; Wang, Y.; Zhu, C.; Liu, J.; Li, J.; Sham, T.-K.; Xu, X.; Zheng, G. Efficient electrocatalytic CO_2 reduction to C_{2+} alcohols at defect-site-rich Cu surface. *Joule* **2021,** *5*, 429-440.

22. Xing, Z.; Hu, L.; Ripatti, D. S.; Hu, X.; Feng, X. Enhancing carbon dioxide gas-diffusion electrolysis by creating a hydrophobic catalyst microenvironment. *Nat. Commun.* **2021,** *12*, 136.

23. Sa, Y. J.; Lee, C. W.; Lee, S. Y.; Na, J.; Lee, U.; Hwang, Y. J. Catalyst-electrolyte interface chemistry for electrochemical CO_2 reduction. *Chem. Soc. Rev.* **2020,** *49*, 6632-6665.

24. Chen, C.; Li, Y.; Yu, S.; Louisia, S.; Jin, J.; Li, M.; Ross, M. B.; Yang, P. Cu-Ag tandem catalysts for high-rate CO_2 electrolysis toward multicarbons. *Joule* **2020,** *4*, 1688-1699.

25. Lyu, Z.; Zhu, S.; Xu, L.; Chen, Z.; Zhang, Y.; Xie, M.; Li, T.; Zhou, S.; Liu, J.; Chi, M.; Shao, M.; Mavrikakis, M.; Xia, Y. Kinetically controlled synthesis of Pd-Cu Janus nanocrystals with enriched surface structures and enhanced catalytic activities toward CO_2 reduction. *J. Am. Chem. Soc.* **2021,** *143*, 149-162.

26. Huang, J.; Mensi, M.; Oveisi, E.; Mantella, V.; Buonsanti, R. Structural sensitivities in bimetallic catalysts for electrochemical CO_2 reduction revealed by Ag-Cu nanodimers. *J. Am. Chem. Soc.* **2019,** *141*, 2490-2499.

27. Herzog, A.; Bergmann, A.; Jeon, H. S.; Timoshenko, J.; Kühl, S.; Rettenmaier, C.; Lopez Luna, M.; Haase, F. T.; Roldán Cuenya, B. Operando investigation of Ag-decorated Cu_2O nanocube catalysts with enhanced CO_2 electroreduction toward liquid products. *Angew. Chem., Int. Ed.* **2021,** *60*, 7426-7435.

28. Xiong, L.; Zhang, X.; Yuan, H.; Wang, J.; Yuan, X.; Lian, Y.; Jin, H.; Sun, H.; Deng, Z.; Wang, D.; Hu, J.; Hu, H.; Choi, J.; Li, J.; Chen, Y.; Zhong, J.; Guo, J.; Rummerli, M. H.; Xu, L.; Peng, Y. Breaking linear scaling relationship by compositional and structural crafting of ternary Cu-Au/Ag nanoframes for electrocatalytic ethylene production. *Angew. Chem., Int. Ed.* **2020,** *60*, 2508-2518.

29. Jia, H.; Yang, Y.; Chow, T. H.; Zhang, H.; Liu, X.; Wang, J.; Zhang, C. y. Symmetry-broken Au–Cu heterostructures and their tandem catalysis process in electrochemical CO_2 reduction. *Adv. Funct. Mater.* **2021,** *31*, 2101255.

30. Ting, L. R. L.; Piqué, O.; Lim, S. Y.; Tanhaei, M.; Calle-Vallejo, F.; Yeo, B. S. Enhancing CO_2 electroreduction to ethanol on copper–silver composites by opening an alternative catalytic pathway. *ACS Catal.* **2020,** *10*, 4059-4069.

31. Morales-Guio, C. G.; Cave, E. R.; Nitopi, S. A.; Feaster, J. T.; Wang, L.; Kuhl, K. P.; Jackson, A.; Johnson, N. C.; Abram, D. N.; Hatsukade, T.; Hahn, C.; Jaramillo, T. F. Improved CO_2 reduction activity towards C_{2+} alcohols on a tandem gold on copper

electrocatalyst. *Nat. Catal.* **2018,** *1*, 764-771.

32. Gao, J.; Zhang, H.; Guo, X.; Luo, J.; Zakeeruddin, S. M.; Ren, D.; Gratzel, M. Selective C-C coupling in carbon dioxide electroreduction via efficient spillover of intermediates as supported by operando Raman spectroscopy. *J. Am. Chem. Soc.* **2019,** *141*, 18704-18714.

33. Lum, Y.; Ager, J. W. Sequential catalysis controls selectivity in electrochemical CO_2 reduction on Cu. *Energy Environ. Sci.* **2018,** *11*, 2935-2944.

34. Iyengar, P.; Kolb, M. J.; Pankhurst, J. R.; Calle-Vallejo, F.; Buonsanti, R. Elucidating the facet-dependent selectivity for CO_2 electroreduction to ethanol of Cu–Ag tandem catalysts. *ACS Catal.* **2021,** *11*, 4456-4463.

35. Ma, S.; Sadakiyo, M.; Heima, M.; Luo, R.; Haasch, R. T.; Gold, J. I.; Yamauchi, M.; Kenis, P. J. A. Electroreduction of carbon dioxide to hydrocarbons using bimetallic Cu–Pd catalysts with different mixing patterns. *J. Am. Chem. Soc.* **2017,** *139*, 47-50.

36. Wang, X.; de Araujo, J. F.; Ju, W.; Bagger, A.; Schmies, H.; Kuhl, S.; Rossmeisl, J.; Strasser, P. Mechanistic reaction pathways of enhanced ethylene yields during electroreduction of CO_2-CO co-feeds on Cu and Cu-tandem electrocatalysts. *Nat. Nanotechnol.* **2019,** *14*, 1063-1070.

37. De Gregorio, G. L.; Burdyny, T.; Loiudice, A.; Iyengar, P.; Smith, W. A.; Buonsanti, R. Facet-dependent selectivity of Cu catalysts in electrochemical CO_2 reduction at commercially viable current densities. *ACS Catal.* **2020,** *10*, 4854-4862.

38. Huang, Y.; Handoko, A. D.; Hirunsit, P.; Yeo, B. S. Electrochemical reduction of CO_2 using copper single-crystal surfaces: Effects of CO* coverage on the selective formation of ethylene. *ACS Catal.* **2017,** *7*, 1749-1756.

39. Calle-Vallejo, F.; Koper, M. T. M. Theoretical considerations on the electroreduction of CO to C_2 species on Cu(100) electrodes. *Angew. Chem., Int. Ed.* **2013,** *52*, 7282-7285.

40. Hahn, C.; Hatsukade, T.; Kim, Y.-G.; Vailionis, A.; Baricuatro, J. H.; Higgins, D. C.; Nitopi, S. A.; Soriaga, M. P.; Jaramillo, T. F. Engineering Cu surfaces for the electrocatalytic conversion of CO_2: Controlling selectivity toward oxygenates and hydrocarbons. *Proc. Natl. Acad. Sci. U. S. A.* **2017,** *114*, 5918-5923.

41. Montoya, J. H.; Shi, C.; Chan, K.; Nørskov, J. K. Theoretical insights into a CO dimerization mechanism in CO_2 electroreduction. *J. Phys. Chem. Lett.* **2015,** *6*, 2032-2037.

42. Schouten, K. J. P.; Qin, Z.; Pérez Gallent, E.; Koper, M. T. M. Two pathways for

the formation of ethylene in CO reduction on single-crystal copper electrodes. *J. Am. Chem. Soc.* **2012,** *134*, 9864-9867.

43. Jiang, K.; Sandberg, R. B.; Akey, A. J.; Liu, X.; Bell, D. C.; Nørskov, J. K.; Chan, K.; Wang, H. Metal ion cycling of Cu foil for selective C–C coupling in electrochemical CO_2 reduction. *Nat. Catal.* **2018,** *1*, 111-119.

44. Loiudice, A.; Lobaccaro, P.; Kamali, E. A.; Thao, T.; Huang, B. H.; Ager, J. W.; Buonsanti, R. Tailoring copper nanocrystals towards C_2 products in electrochemical CO_2 reduction. *Angew. Chem., Int. Ed.* **2016,** *55*, 5789-5792.

45. Schouten, K. J. P.; Pérez Gallent, E.; Koper, M. T. M. Structure sensitivity of the electrochemical reduction of carbon monoxide on copper single crystals. *ACS Catal.* **2013,** *3*, 1292-1295.

46. Zhu, Y.; Cui, X.; Liu, H.; Guo, Z.; Dang, Y.; Fan, Z.; Zhang, Z.; Hu, W. Tandem catalysis in electrochemical CO_2 reduction reaction. *Nano Res.* **2021**, DOI: 10.1007/s12274-021-3448-2.

47. Chang, Z.; Huo, S.; Zhang, W.; Fang, J.; Wang, H. The tunable and highly selective reduction products on Ag@Cu bimetallic catalysts toward CO_2 electrochemical reduction reaction. *J. Phys. Chem. C* **2017,** *121*, 11368-11379.

48. Kim, N. R.; Shin, K.; Jung, I.; Shim, M.; Lee, H. M. Ag–Cu bimetallic nanoparticles with enhanced resistance to oxidation: A combined experimental and theoretical study. *J. Phys. Chem. C* **2014,** *118*, 26324-26331.

49. Ye, C.; Peng, M.; Cui, T.; Tang, X.; Wang, D.; Jiao, M.; Miller, J. T.; Li, Y. Revealing the surface atomic arrangement of noble metal alkane dehydrogenation catalysts by a stepwise reduction-oxidation approach. *Nano Res.* **2021**, DOI: 10.1007/s12274-021-3636-0.

50. Ye, C.; Peng, M.; Wang, Y.; Zhang, N.; Wang, D.; Jiao, M.; Miller, J. T. Surface hexagonal Pt_1Sn_1 intermetallic on Pt nanoparticles for selective propane dehydrogenation. *ACS Appl. Mater. Interfaces* **2020,** *12*, 25903-25909.

51. Rosen, B. A.; Salehi-Khojin, A.; Thorson, M. R.; Zhu, W.; Whipple, D. T.; Kenis, P. J. A.; Masel, R. I. Ionic liquid–mediated selective conversion of CO_2 to CO at low overpotentials. *Science* **2011,** *334*, 643-644.

52. Li, F.; Li, Y. C.; Wang, Z.; Li, J.; Nam, D.-H.; Lum, Y.; Luo, M.; Wang, X.; Ozden, A.; Hung, S.-F.; Chen, B.; Wang, Y.; Wicks, J.; Xu, Y.; Li, Y.; Gabardo, C. M.; Dinh, C.-T.; Wang, Y.; Zhuang, T.-T.; Sinton, D.; Sargent, E. H. Cooperative CO_2-to-ethanol conversion via enriched intermediates at molecule–metal catalyst interfaces. *Nat. Catal.*

2019, *3*, 75-82.

53. Schouten, K. J. P.; Kwon, Y.; van der Ham, C. J. M.; Qin, Z.; Koper, M. T. M. A new mechanism for the selectivity to C_1 and C_2 species in the electrochemical reduction of carbon dioxide on copper electrodes. *Chem. Sci.* **2011,** *2*, 1902-1909.

54. Goodpaster, J. D.; Bell, A. T.; Head-Gordon, M. Identification of possible pathways for C–C bond formation during electrochemical reduction of CO_2: New theoretical insights from an improved electrochemical model. *J. Phys. Chem. Lett.* **2016,** *7*, 1471-1477.

55. Ren, W.; Zhao, C. Paths towards enhanced electrochemical CO_2 reduction. *Natl. Sci. Rev.* **2019,** *7*, 7-9.

56. Li, J.; Wang, Z.; McCallum, C.; Xu, Y.; Li, F.; Wang, Y.; Gabardo, C. M.; Dinh, C.-T.; Zhuang, T.-T.; Wang, L.; Howe, J. Y.; Ren, Y.; Sargent, E. H.; Sinton, D. Constraining CO coverage on copper promotes high-efficiency ethylene electroproduction. *Nat. Catal.* **2019,** *2*, 1124-1131.

FIGURES

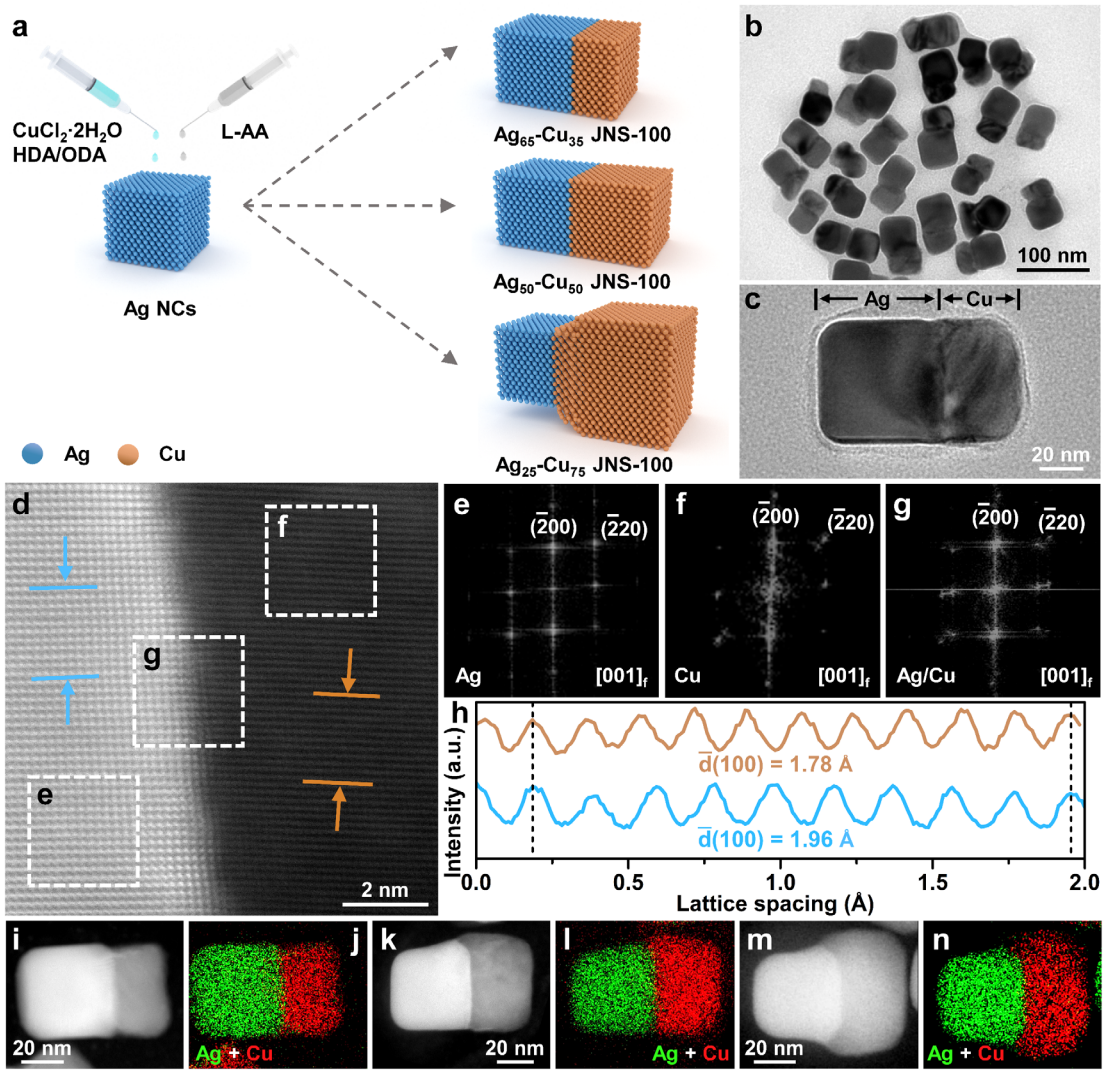

Figure 1. Synthesis and structural characterization of Ag-Cu JNS-100. (a) Schematic illustration for the synthesis of three kinds of Ag-Cu JNS-100 via confined growth of Cu on only one of the six equal faces of Ag NCs. HDA, 1-hexadecylamine; ODA, octadecylamine; L-AA, L-ascorbic acid. (b,c) TEM images of Ag_{65}-Cu_{35} JNS-100. (d) Spherical aberration-corrected high-resolution HAADF-STEM image of Ag/Cu interface in Ag_{65}-Cu_{35} JNS-100. (e-g) FFT patterns of the selected Ag domain (e), Cu domain (f) and Ag/Cu interface (g) in (d). (h) The integrated pixel intensities of Cu (orange curve) and Ag (sky-blue curve) along the arrow directions of the selected areas in (d). The valleys and peaks represent the alternating voids and atoms, respectively. (i-n) HAADF-STEM images (i,k,m) and EDS elemental mappings (j,l,n) of Ag_{65}-Cu_{35}, Ag_{50}-Cu_{50} and Ag_{25}-Cu_{75} JNS-100, respectively.

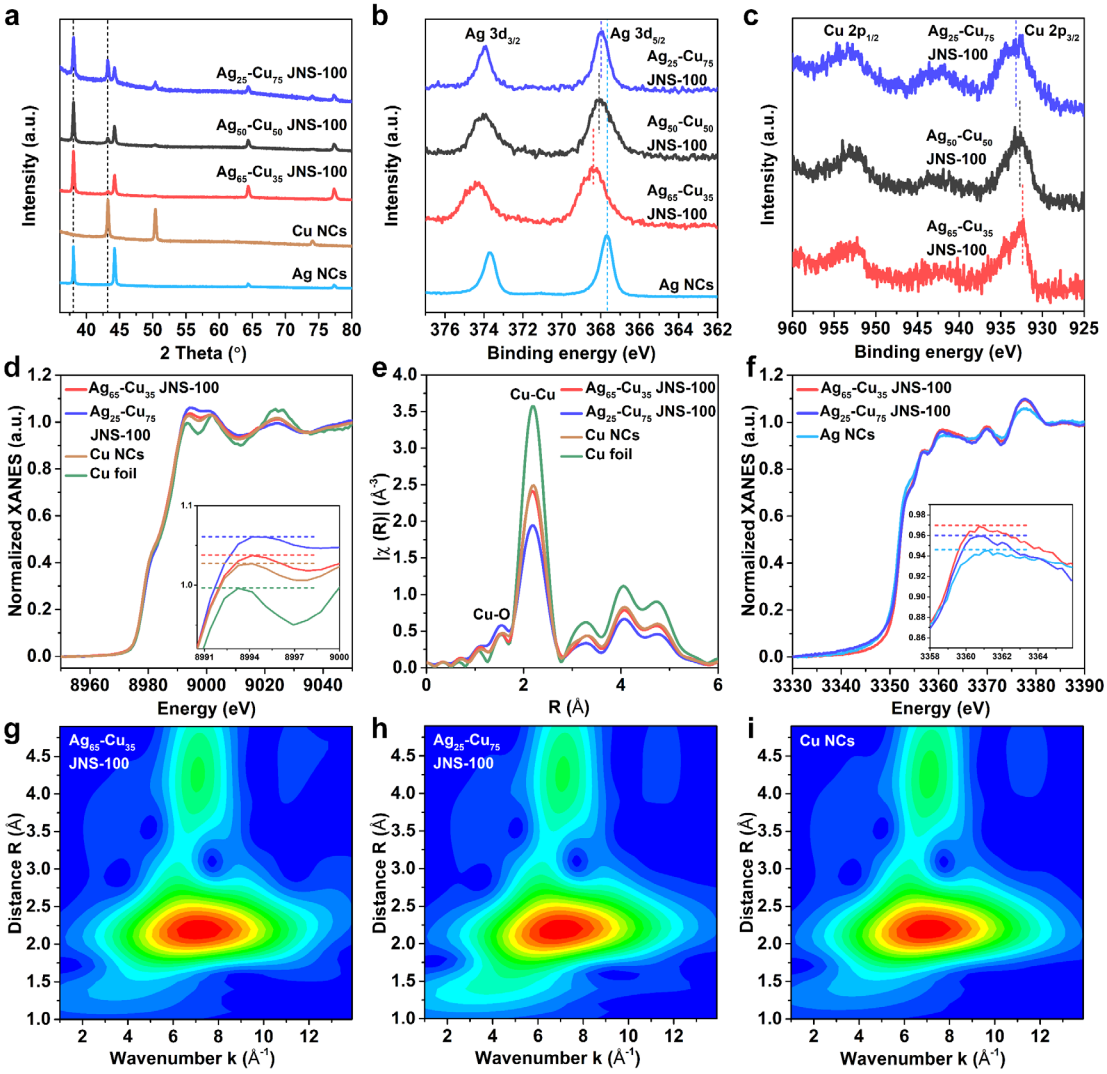

Figure 2. X-ray spectral analysis of Ag-Cu JNS-100. (a) XRD patterns of Ag_{65}-Cu_{35} JNS-100, Ag_{50}-Cu_{50} JNS-100, Ag_{25}-Cu_{75} JNS-100, Ag NCs and Cu NCs. (b) XPS spectra of Ag 3d in Ag_{65}-Cu_{35} JNS-100, Ag_{50}-Cu_{50} JNS-100, Ag_{25}-Cu_{75} JNS-100 and Ag NCs. (c) XPS spectra of Cu 2p in Ag_{65}-Cu_{35}, Ag_{50}-Cu_{50} and Ag_{25}-Cu_{75} JNS-100. (d) Normalized XANES and the enlarged white line (the inset) spectra of Cu K edge in Ag_{65}-Cu_{35} JNS-100, Ag_{25}-Cu_{75} JNS-100, Cu NCs and Cu foil. (e) Cu K edge EXAFS spectra of Ag_{65}-Cu_{35} JNS-100, Ag_{25}-Cu_{75} JNS-100, Cu NCs and Cu foil. (f) Normalized XANES and the enlarged white line (the inset) spectra of Ag L_3 edge in Ag_{65}-Cu_{35} JNS-100, Ag_{25}-Cu_{75} JNS-100 and Ag NCs. (g-i) Wavelet transform of Cu K edge EXAFS of Ag_{65}-Cu_{35} JNS-100 (g), Ag_{25}-Cu_{75} JNS-100 (h) and Cu NCs (i).

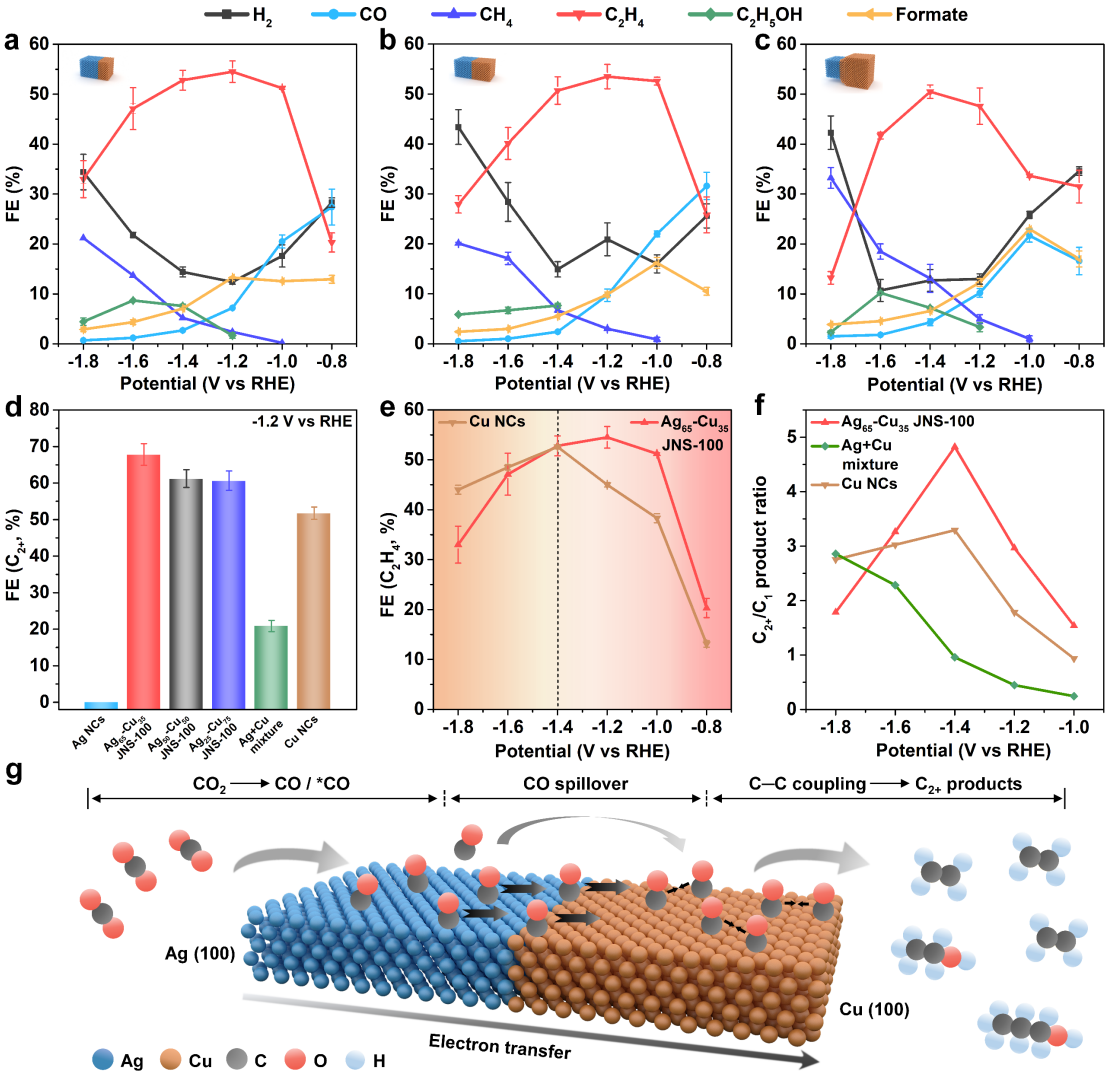

Figure 3. CO_2RR performance of Ag-Cu JNS-100. (a-c) FE of major CO_2-reduction products obtained on Ag_{65}-Cu_{35} JNS-100 (a), Ag_{50}-Cu_{50} JNS-100 (b) and Ag_{25}-Cu_{75} JNS-100 (c) at different potentials. (d) FE of C_{2+} products obtained on Ag NCs, Ag_{65}-Cu_{35} JNS-100, Ag_{50}-Cu_{50} JNS-100, Ag_{25}-Cu_{75} JNS-100, Ag+Cu mixture and Cu NCs at -1.2 V (vs RHE). (e) Comparison of C_2H_4 FE between Ag_{65}-Cu_{35} JNS-100 and Cu NCs at different potentials. (f) Comparison of C_{2+}/C_1 product ratios between Ag_{65}-Cu_{35} JNS-100, Ag+Cu mixture and Cu NCs. (g) Schematic illustration of a plausible CO_2RR mechanism on Ag_{65}-Cu_{35} JNS-100.

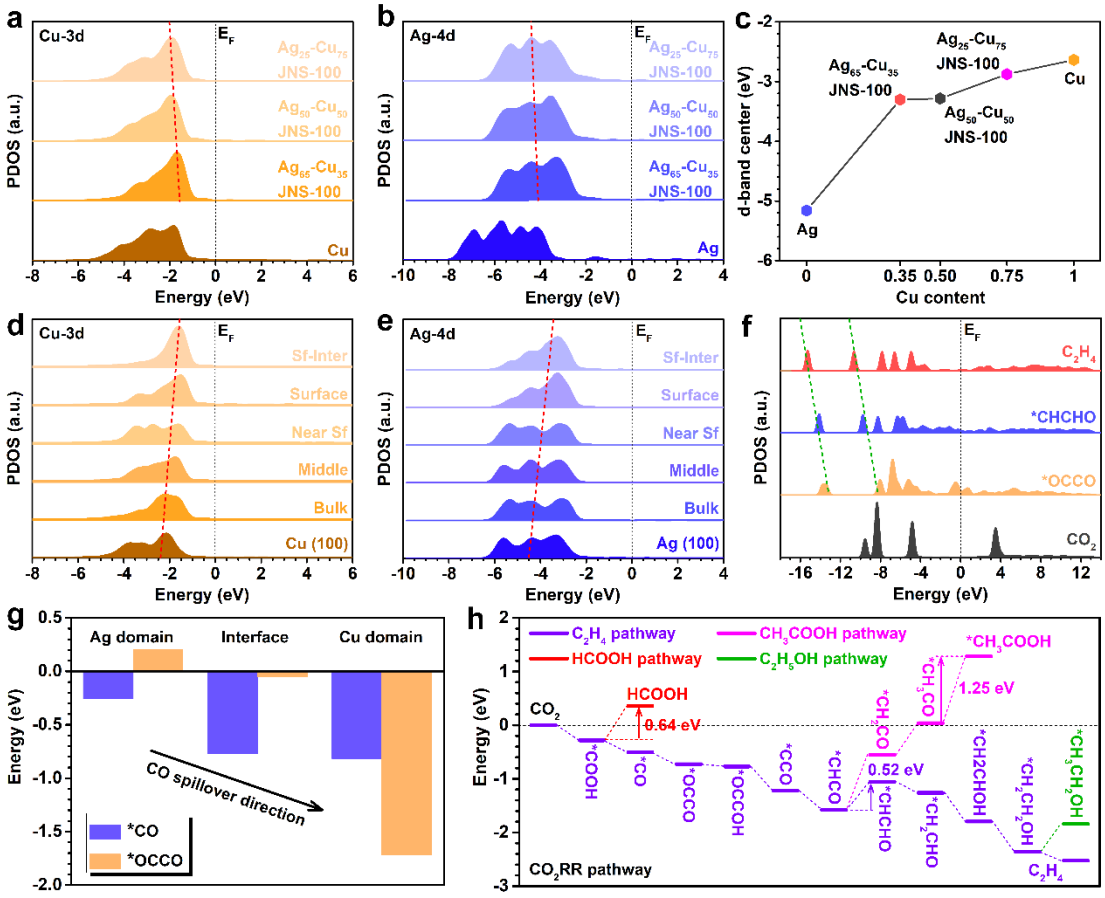

Figure 4. Theoretical calculations of electrocatalytic CO_2RR on Ag-Cu JNS-100. (a,b) The PDOS comparison of Cu-3d (a) and Ag-4d (b) in Ag_{65}-Cu_{35}, Ag_{50}-Cu_{50} and Ag_{25}-Cu_{75} JNS-100. (c) The d-band center comparison between Ag, Ag_{65}-Cu_{35} JNS-100, Ag_{50}-Cu_{50} JNS-100, Ag_{25}-Cu_{75} JNS-100 and Cu. (d,e) The site-dependent PDOS of Cu-3d (d) and Ag-4d (e) in Ag_{65}-Cu_{35} JNS-100. (f) The PDOS comparison of key adsorbates in CO_2RR toward C_2H_4. (g) The adsorption energies of *CO and *OCCO on different sites of Ag_{65}-Cu_{35} JNS-100. (h) The reaction trend of different CO_2RR pathways on Ag_{65}-Cu_{35} JNS-100.